Mid-Infrared Ellipsometry for Optical Critical Dimension Metrology

G. Andrew Antonelli, Troy. D. Ribaudo, and Nick Keller
Onto Innovation Inc. 16 Jonspin Road, Wilmington, MA 01887.

(*Electronic mail: nicholas.keller@ontoinnovation.com)

(Dated: 30 December 2025)

Mid-infrared ellipsometry offers a powerful approach for non-destructive optical critical dimension (OCD) metrology in advanced semiconductor manufacturing. This technique supports in-line measurements of high aspect ratio structures, such as those found in 3D NAND memory devices. The incorporation of quantum cascade lasers and fast phase modulation allows rapid acquisition of Mueller matrix elements with high spatial resolution and sub-Å precision. Material-specific absorption in the mid-infrared range allows depth-resolved profiling of device structures, overcoming the limitations of conventional OCD. Rigorous coupled wave analysis (RCWA) is used to extract structural parameters from the measured spectra. Agreement with destructive reference metrology has been demonstrated on a variety of structures. The ability to measure multiple Mueller elements further enhances characterization of complex geometries, making mid-infrared ellipsometry a valuable tool for process control in semiconductor fabrication.

I. INTRODUCTION

Controlling the myriad of variables involved in the manufacture of advanced semiconductor devices requires a multitude of measurements between each processing operation[1,2]. Geometric fidelity and thus the measurement of critical dimensions is one of the most important. A small number of representative samples can be extracted from the manufacturing flow for destructive analysis in offline laboratory techniques such as transmission electron microscopy (TEM)[3]. Non-destructive in-line measurement is preferred as it allows a faster response to a process excursion and thus limits product loss[4].

Electron beam and optical equipment are both used for in-line characterization of critical dimensions. Critical dimension Scanning electron microscopy (CD-SEM) systems are used for examining the fine details of in-plane device patterns, and although significant progress has been made in extending these technology to three-dimensional structures using high-voltage methods these tools are predominantly used for the analysis of two-dimensional or near surface pattern variation[5,6]. Optical imaging methods are in general subject to diffraction and are thus capable of only extracting information from structures larger than the wavelengths of the optical source. There are a number of near-field optical systems that skirt this requirement but the speed with which these tools operate can be an issue for use for in-line measurement[7,8]. Non-imaging optical methods based on scatterometry and termed optical critical dimension (OCD) metrology have been shown to be capable of non-destructive three-dimension critical dimension extraction in complex devices at high throughput with results that agree well with destructive reference methods[9–11].

Modern OCD tools are essentially a fixed oblique angle spectroscopic ellipsometer, normal incidence polarized reflectometer, or a combination of the two with an optical spot size less than 30 µm and full spectral measurements completed on a given site in < 1 s[12]. Polarized reflectometry provides two data channels from the polarization state. Shift of ellipsometry from a two, Ψ-Δ, to 15 elements, normalized full Mueller matrix, has enabled the analysis of more complex structures[13]. The other key driver for advancement is expansion of wavelength range[14,15]. This growth has been largely accretive growing from the visible out into the deep ultraviolet and near infrared. The introduction and refinement of compact laser driven light sources (LDLS) capable of integration into existing OCD systems has been the most recent innovation[16]. In addition to the expansion in the spectral range, the LDLS enabled a reduction in the physical spot size of the instrument through an increase in brightness and decrease in optical source size allowing the optimization of the etendue of the optical system without impacting the signal to noise ratio[17]. The source of light in an LDLS is a ball of plasma, 50 µm in diameter, maintained by a laser inside a glass bulb filled with a mixture of gases. This size is multiple orders of magnitude smaller than the filament of an incandescent bulb or the electrode spacing, arc, in an arc lamp.

Metrology tools operating in the mid-infrared are used for in-line monitoring in semiconductor manufacturing. Fourier transform infrared spectroscopy (FTIR) is ubiquitous in semiconductor development[18]. Manual and fully automated wafer-handling systems with a probe size diameter between 1 mm-5 mm with data acquisition times <30 s are available from many suppliers. These tools are used for compositional analysis of blanket thin films deposited on semiconducting wafers or the wafers themselves through transmission or reflection measurements[19–22]. Model-based infrared reflectometry (MBIR) is an associated FTIR implementation intended to operate only in reflection and having a probe diameter from 1 mm to 50 µm with the signal level decreasing with probe diameter and thus longer acquisition time required[23]. Although MBIR can be used to determine composition especially on product wafers with test pad sizes <50 µm, it is more commonly applied to the determination of the critical dimensions of high aspect ratio (HAR) structures using an effective medium approximation to determine structural parameters[24–27].

An FTIR instrument can be modified to create an ellipsometer by introducing polarization state generators at appropriate points in the optical system. There is a significant body of academic literature describing this configuration[28], and the Woollam IR-VASE™ is a commercially available realization[29,30].

However, mid-infrared ellipsometers need not be based on an FTIR[31]. This alternative configuration has historically had a simple optical layout but low signal to noise ratio due to the weakness of the light source. Although other types of light sources including plasmas and synchrotrons, the source in almost all of these commercial infrared instruments is a glowbar which is a silicon carbide rod heated to >1000 °C and acts as Planck radiator. They are low noise but present an etendue issue limiting the ability to capture the radiated energy[32,33]. In this situation, long acquisition times of many hours may be required to make useful measurements. Just as the LDLS was a boon for OCD in the deep ultraviolet and near-infrared, new source technologies have allowed expansion of ellipsometry into the mid-infrared, 3 µm to 30 µm, range and the use of this method for in-line measurements[34–37].

II. METHODS

A. Apparatus

The Aspect ® technology developed by Onto Innovation is a mid-infrared ellipsometer that does not rely on a FTIR spectrometer[37]. Instead of a glowbar, it uses a tunable quantum-cascade laser (QCL) with an operating range of about 5.2 µm to 11.1 µm or 1923 cm^{-1} to 901 cm^{-1}.

The optical system after the laser consists of an amplitude modulator such as a mechanical chopper followed by an illuminator and a receiver assembly. Both the former and later have a wire grid polarizer, wire array deposited on a silicon blank, that can be rotated to an arbitrary angle and fixed, i.e., polarizer and analyzer. The illuminator has a variable retarder after the polarizer. A photo-elastic modular (PEM) rather than a rotating element is used as the variable retarder. The resonant frequency of the PEM depends on the material and how the the crystal is cut. In this case, the material is zinc selenide and the frequency is 50 kHz.

Schwarzschild objectives with a gold coating are used to focus the light onto the sample at an oblique angle of incidence, >45°, from the illuminator assembly and recollimate the light entering the receiver assembly. The currently available system has a probe size of <50 µm by 150 µm much smaller than other ellipsometers operating in this wavelength range. The light is finally directed onto a monolithic mercury cadmium-telluride (MCT) detector with thermoelectric cooling allowing operation down to 14 µm. The measurement time, which includes the overhead for stage motion, focusing, and pattern recognition, across the available spectral range of the QCL at >1000 individual wavenumbers is < 10 s for the current configuration with a single variable retarder in the illuminator allowing extraction of two Mueller matrix elements. By adding a second variable retarder into the receiver assembly, eight Mueller matrix elements can be determined with no change in probe size or measurement time. Neither the QCL scan rate nor the frequency of the variable retarder limit the current measurement time. A substantial reduction in measurement time may be realized in future systems through further system optimization and overhead reduction bringing this system's measurement time closer to that of more conventional OCD systems.

The system operates by discretely scanning QCL through its spectral range and sequentially capturing data from detector. The signal at the detector has been amplitude modulated by the mechanical chopper and phase modulated by the PEM between the polarizer, sample, and analyzer. The detector mentioned should be designed such that there is a flat-band condition in its frequency response compatible with these two modulations. The signal is then demodulated using lock-in-amplifiers and the ellipsometeric parameters extracted.

The PEM voltage for this instrument is set at a fixed value and is not changed as a function of wavelength. This approach is similar to what is used in polarization modulation FTIR systems[38,39]. The scanning of the QCL is analogous to the scanning of the interferometer in the FTIR. Fixing the voltage ensures stability but also implies that the retardance will vary as a function of wavelength. A method of extracting the retardance function is thus fundamental to the operation of the instrument.

B. System Model of Apparatus

To better understand the data processing, it is instructive to build a system model of the ellipsometer following the approach developed by Jellison[40]. The normalized input Stokes vector from the light source is taken to be linearly polarized,

$$S_{in} = \begin{pmatrix} 1 \\ \cos(2\alpha) \\ \sin(2\alpha) \\ 0 \end{pmatrix}, \tag{1}$$

where α is the angle of the polarization relative to the optical table horizontal. The Mueller matrix for the polarizer and analyzer is given by:

$$M_{pol} = \frac{1}{2}\begin{pmatrix} \left(p_x^2+p_y^2\right) & \cos(2\beta)\left(p_x^2-p_y^2\right) & \sin(2\beta)\left(p_x^2-p_y^2\right) & 0 \\ \cos(2\beta)\left(p_x^2-p_y^2\right) & \left(\cos^2(2\beta)\left(p_x^2+p_y^2\right)+2p_xp_y\sin^2(2\beta)\right) & \sin(2\beta)\cos(2\beta)\left(p_x^2-2p_xp_y+p_y^2\right) & 0 \\ \sin(2\beta)\left(p_x^2-p_y^2\right) & \sin(2\beta)\cos(2\beta)\left(p_x^2-2p_xp_y+p_y^2\right) & \left(\sin^2(2\beta)\left(p_x^2+p_y^2\right)+2p_xp_y\cos^2(2\beta)\right) & 0 \\ 0 & 0 & 0 & 2p_xp_y \end{pmatrix}, \tag{2}$$

where β is the angle of orientation, and p_x and p_y are the amplitude of the attenuation coefficients. p_x^2 and p_y^2 with

$p^2 = p_x^2 + p_y^2$ are the observed intensity transmittances with x representing horizontal polarization and y vertical. $p = 1$ for an ideal polarizer. These parameters are determined experimentally by transmission measurements and will vary wavelength. The photo-elastic modulator can be represented by the Mueller matrix:

$$M_{PEM} = \begin{pmatrix} 1 & 0 & 0 & 0 \\ 0 & \cos(d)\sin^2(2\gamma)+\cos^2(2\gamma) & (1-\cos(d))\sin(2\gamma)\cos(\gamma) & \sin(d)\sin(2\gamma) \\ 0 & (1-\cos(d))\sin(2\gamma)\cos(2\gamma) & \cos(d)\cos^2(2\gamma)+\sin^2(2\gamma) & \sin(d)(-\cos(2\gamma)) \\ 0 & -\sin(d)\sin(2\gamma) & \sin(d)\cos(2\gamma) & \cos(d) \end{pmatrix}, \tag{3}$$

where γ is the orientation angle of the PEM relative to the optical table and d the retardance with,

$$d = d_0 + a\cos(\omega t), \tag{4}$$

where d_0 is the static retardance, a is the dynamic retardance, $\omega = 2\pi f$ is the resonance frequency of the PEM, and t is time. a is proportional to the amplitude of the resonance induced in the PEM and thus the applied voltage. The sample being measured is assumed for now to have the form:

$$M_S = \begin{pmatrix} 1 & -N & 0 & 0 \\ -N & 1 & 0 & 0 \\ 0 & 0 & C & S \\ 0 & 0 & -S & C \end{pmatrix}, \tag{5}$$

where $N = \cos(2\Psi)$, $C = \sin(2\Psi)\sin(\Delta)$, $S = \sin(2\Psi)\cos(\Delta)$ with Ψ and Δ representing respectively the amplitude ratio and phase difference between the p and s components of polarization.

With these definitions, a simple system model for the described ellipsometer can be written as:

$$S_{out} = M_{pol}(\theta_A)M_S M_{PEM}(\theta_{PEM})M_{pol}(\theta_P)S_{in}(\theta_{ls}), \tag{6}$$

where θ_A, θ_{PEM}, and θ_P are the angles of rotation of the components relative to the optical table and θ_{ls} is the polarization of the light output from the light source assembly. In what follows, these angles will be set to $-\frac{\pi}{4}$, 0, $\frac{\pi}{4}$, and $\frac{\pi}{4}$.

The M_{PEM} with the dynamic retardation term will contain terms which can be expanded using the identities:

$$\sin(a\cos(\omega t)) = -2\sum_{n=1}^{\infty}(-1)^n J_{2n-1}(a)\cos((2n-1)\omega t) \tag{7}$$

$$\cos(a\cos(\omega t)) = J_0(a) + 2\sum_{n=1}^{\infty}(-1)^n J_{2n}(a)\cos(2n\omega t). \tag{8}$$

Assuming the polarizers are ideal and using equation 6, the normalized intensity after the analyzer to second order in frequency will be:

$$\begin{aligned} I = \frac{1}{4}(1 + J_0(a)(\cos(d_0)C + \sin(d_0)S) - \\ 2J_1(a)(\sin(d_0)C - \cos(d_0)S)\cos(\omega t) - \cdot \\ 2J_2(a)(\cos(d_0)C + \sin(d_0)S)\cos(2\omega t)) \end{aligned} \tag{9}$$

Equation 9 consists of a static term and ones proportional to the first and second harmonic of the fundamental frequency of the PEM. As indicated in subsection II A, the amplitude of the light source was modulated. The modulation will be assumed periodic with frequency f_{AM}. By selecting $f_{AM} \neq nf$ where $n \in \mathbf{N}$, these three terms can be extracted by monitoring the intensity at f_{AM}, f, and $2f$ with the detector. It should be noted that the amplitude modulation is not technically required. In principle, it is possible to simply measure the constant term as a DC offset. However, MCT detectors are in general AC coupled due to the potential sources of error associated with DC signals[41]. For this reason, the amplitude modulation approach was used on this instrument.

Forming the ratios of the signals with even and odd harmonics of the PEM to the signal of the amplitude modulation and solving for C and S,

$$C = -\frac{J_1(a)S_{2f}\cos(d_0) + J_2(a)S_{1f}\sin(d_0)}{J_1(a)(2J_2(a)S_{AM} + J_0(a)S_{2f})} \tag{10}$$

$$S = -\frac{J_1(a)S_{2f}\sin(d_0) - J_2(a)S_{1f}\cos(d_0)}{J_1(a)(2J_2(a)S_{AM} + J_0(a)S_{2f})}. \tag{11}$$

The addition of a proportionality constant may be necessary depending on the detection method and waveform used for amplitude modulation[42]. The measured signals are extracted using a lock-in amplifier and are thus root mean square values. The factor of $\frac{1}{\sqrt{2}}$ would be canceled by the ratio of the signals. When a mechanical chopper is used for amplitude modulation, a factor $\frac{\pi}{4}$, is needed to account for the lock-in amplifier extracting the fundamental of the square wave. If the waveform deviates from a square wave due to improper setup of the chopper relative to the beam, the required factor will deviate, but provided the optical setup is fixed it can be experimentally determined. For these measurements, the ideal value was found to work well.

Returning the method of detection, the lock-in amplifier is phase sensitive, and the units used are capable of outputting a magnitude and phase for all quantities. The phase of the amplitude modulation has no impact on the analysis. However, the phase of the harmonic quantities must be tracked to account for shifts in π due to a change in the sign of the ellipsometeric parameters.

Under the assumption that $N^2 + C^2 + S^2 = 1$, the N can also be extracted from this analysis. It is a useful extraction to perform for certain samples as it allows one to verify the quality of the calibration. However, it is not advised to use this value when fitting modeled results as the error in N depends in a non-linear fashion on the values of C and S as well as the

error in those parameters,

$$\delta N = -\frac{C\delta C + S\delta S}{\sqrt{1-C^2-S^2}}. \tag{12}$$

Further investigation of Equation 9 at higher harmonics will show that all odd and even harmonics will have the same prefactors. This feature can be used in the calibration of the instrument[43]. By measuring the ratio of any two odd or even harmonics on a sample and fitting the ratio of the two harmonics to the ratio of the relevant Bessel functions, the dynamic retardance a of the PEM can be extracted as a function of wavelength. For example, if the first and third harmonics were selected,

$$\frac{S_{1f}}{S_{3f}} = \frac{J_1(a)}{J_3(a)}. \tag{13}$$

This method of calibration may be performed in-situ in the reflection configuration as opposed to other methods based on transmission[40]. Further, this calibration can be automated to account for drift in the PEM.

Equation 5 assumes that the sample can be described by a NCS paramaterization which is a good assumption for many structures but is not always the case. If instead, the sample is assumed to have the form of the most general normalized Mueller matrix:

$$M_S = \begin{pmatrix} 1 & M_{12} & M_{13} & M_{14} \\ M_{21} & M_{22} & M_{23} & M_{24} \\ M_{31} & M_{32} & M_{33} & M_{34} \\ M_{41} & M_{42} & M_{43} & M_{44} \end{pmatrix}. \tag{14}$$

In this case, C and S or more correctly M_{33} and M_{34} are replaced by a combination of Mueller matrix elements. Extracting the signals using amplitude modulation and forming the ratio of the signals will again lead to Equation 11 with C and S replaced by C_{MM} and S_{MM} respectively:

$$C_{MM} = \frac{M_{33}+M_{13}}{1+M_{31}} \tag{15}$$

$$S_{MM} = \frac{M_{34}+M_{14}}{1+M_{31}}. \tag{16}$$

If the off-diagonal Mueller elements are zero, equations 15 and 16 revert to M_{33} and M_{34} as expected.

The addition of second variable retarder, PEM, in the receiver arm before the analyzer allows the extraction of 8 Mueller matrix elements an analysis of this configuration has been extensively reviewed by Jellison[44,45]. The system model for this configuration would be described by:

$$\begin{aligned} S_{out} =& M_{pol}(\theta_A) M_{PEM2}(\theta_{PEM2}) M_S \times \\ & M_{PEM1}(\theta_{PEM1}) M_{pol}(\theta_P) S_{in}(\theta_{ls}), \end{aligned} \tag{17}$$

where the two PEM units must necessarily have different resonant frequencies: f_1 and f_2. For the sake of simplicity, the angle for the second PEM will be set to 0 and the other components will retain their previous values. The intensity can again be broken down into a series of frequency components. In this case, the frequencies of the two PEMs will mix. The user must select a complete set of frequencies but has some freedom in doing so as discussed by Jellison[44]. Under the current assumptions expanding only to second order in frequency, one set of complete equations is:

$$\begin{aligned}
I_{AM} &= \frac{1}{2}(1 + J_0(a_1)(M_{13}\cos(d_{01}) + M_{14}\sin(d_{01}) + \\
&\quad J_0(a_1)\cos(d_{01})J_0(a_2)(M_{33}\cos(d_{02}) - M_{43}\sin(d_{02})) + \\
&\quad J_0(a_1)\sin(d_{01})J_0(a_2)(M_{34}\cos(d_{02}) - M_{44}\sin(d_{02}) + \\
&\quad J_0(a_2)(M_{31}\cos(d_{02}) - M_{41}\sin(d_{02})))\\
I_{11} &= J_1(a_1)((-M_{13}\sin(d_{01} + M_{14}\cos(d_{01})) - \\
&\quad \sin(d_{01})(J_0(a_2)(M_{33}\cos(d_{02}) - M_{43}\sin(d_{02}))) + \\
&\quad \cos(d_{01})(J_0(a_2)(M_{34}\cos(d_{02}) - M_{44}\sin(d_{02})))\\
I_{12} &= -J_1(a_2)((M_{31}\sin(d_{02} + M_{41}\cos(d_{02})) + \\
&\quad \sin(d_{02})(J_0(a_1)(M_{33}\cos(d_{01}) + M_{34}\sin(d_{01}))) + \\
&\quad \cos(d_{02})(J_0(a_1)(M_{43}\cos(d_{01}) + M_{44}\sin(d_{01})))\\
I_{21} &= -J_2(a_1)((M_{14}\sin(d_{01} + M_{13}\cos(d_{01})) + \\
&\quad \sin(d_{01})(J_0(a_2)(M_{33}\cos(d_{02}) - M_{43}\sin(d_{02}))) + \\
&\quad \cos(d_{01})(J_0(a_2)(M_{34}\cos(d_{02}) - M_{44}\sin(d_{02})))\\
I_{22} &= -J_2(a_2)((-M_{41}\sin(d_{02} + M_{31}\cos(d_{02})) - \\
&\quad \sin(d_{02})(J_0(a_1)(M_{43}\cos(d_{01}) + M_{44}\sin(d_{01}))) + \\
&\quad \cos(d_{02})(J_0(a_1)(M_{33}\cos(d_{01}) + M_{34}\sin(d_{01})))\\
I_{1112} &= 2J_1(a_1)J_1(a_2)(\sin(d_{01})(M_{43}\cos(d_{02}) + M_{33}\sin(d_{02})) - \\
&\quad \cos(d_{01})(M_{44}\cos(d_{02}) + M_{34}\sin(d_{02}))\\
I_{1122} &= 2J_1(a_1)J_2(a_2)(\sin(d_{01})(M_{33}\cos(d_{02}) - M_{43}\sin(d_{02})) - \\
&\quad \cos(d_{01})(M_{34}\cos(d_{02}) - M_{44}\sin(d_{02}))\\
I_{1221} &= 2J_1(a_2)J_2(a_1)(\sin(d_{01})(M_{44}\cos(d_{02}) + M_{34}\sin(d_{02})) + \\
&\quad \cos(d_{01})(M_{43}\cos(d_{02}) + M_{33}\sin(d_{02}))\\
I_{2122} &= 2J_2(a_1)J_2(a_2)(\sin(d_{01})(M_{33}\cos(d_{02}) - M_{43}\sin(d_{02})) + \\
&\quad \cos(d_{01})(M_{34}\cos(d_{02}) - M_{44}\sin(d_{02})),
\end{aligned} \tag{18}$$

where $\{a_1,d_{01}\}$ and $\{a_2,d_{02}\}$ are respectively the dynamic and static retardance of the illuminator and receiver PEM. I_{AM} is the amplitude modulated component, I_{ij} are the first and second harmonic of the two PEMS, and I_{ijkl} are mixtures of the harmonics of the two PEMs. For example, I_{11} is the first harmonic of the the illuminator PEM, and I_{1122} is the mixture of the first harmonic of the illuminator PEM with the second harmonic of the receiver PEM. There are many ways of extracting the signals, but in the prototype constructed again lock-in-amplifiers were used with at least 9 channels[44,46]. Inverting these equations allows the extraction of 8 Mueller matrix elements chosen by this geomtry to be: $\{M_{33}, M_{34}, M_{43}, M_{44}, M_{13}, M_{14}, M_{31}, M_{41}\}$.

The preceding results derived are representative of the approach used to build a system model of this instrument; however, they are far from complete. Deviations in polarizer angle, rotation of the phase modulator, alignment of system, angular spread induced in the focusing elements, component retardation, impact of coatings, and many other factors must be included to properly calibrate this system[40,44,45,47,48]. But

the methodology is straightforward as these complications are added to equation 6 in the same way that an additional phase modulator was added to equation 17. The analytical approach can even be abandoned in favor of purely numerical method. But in so doing the practitioner looses an understanding of the symmetry of the problem. Instead, one can make use of symbolic computation packages like Wolfram Mathematica to perform symbolic calculations[49]. These analytical results can then be translated into a given computer language like C++. This union of symbolic and numerical computation is extremely powerful and allows the construction of results that would be unlikely to be performed by a human without error.

C. Data Analysis

After appropriate calibration, the data output by the hardware is a set of Mueller matrix elements as a function of wavelength. This data can be analyzed for stacks of thin films on a substrate using the Fresnel equations. For more complex three-dimensional patterned structures, rigorous coupled wave analysis (RCWA) is used[9,11,12]. RCWA is a foundational computation method for extracting the critical dimensions and electromagnetic field for a wide variety of materials and structures[50–53]. However, other electromagnetic modeling techniques like finite-difference time-domain (FDTD) and finite-difference frequency-domain (FDFD) have also found application[54,55]. In this study, the analysis was performed using Ai Diffract^{TM} which is a modeling software developed by Onto Innovation Inc. as part of its OCD solutions suite. This software implements a proprietary RCWA engine optimized for precision and time to solution for complex semiconductor device structures.

For modeling of high aspect ratio structures, like holes or trenches in 3D NAND, a highly robust and flexible method has been developed to parameterize the vertical profile by using orthogonal polynomials. Ai Diffract^{TM} has built-in capability to allow for floating coefficients of N number of polynomial orders and the ability to couple coefficients with coupling equations. Using orthogonal polynomials enables matching complex vertical profiles with a minimal number of free floating parameters compared to using multiple trapezoids or even splines.

Uncertainty and sensitivity analysis is a critical tool in development of OCD models. It is based on Bayesian analysis, where the inputs are spectral noise and parameter sensitivity (extracted by the partial derivatives of every spectral component with respect to every floating parameter)[56]. The output of the analysis is a probability density function for every parameter, denoted by a standard deviation, as well as the corresponding orthogonal uncertainty and degree of correlation. Two-dimensional and three-dimensional parameter correlation tables are also output by the analysis. This analysis allows for predicting measurement performance for all parameters and allows for the user to optimize the model in many different ways (including parameter coupling, fixing parameters, extending or reducing wavelength ranges of various data channels and adjusting data channel weighting).

III. RESULTS

Mid-infrared ellipsometry has a wide variety of applications especially in the analysis of the material properties of samples with strong absorption in this optical range[30]. However, it also offers a unique capability to extract the critical dimensions of high aspect ratio structures like the ones found in 3D NAND memory devices. Figure 1 contains three specific use cases for etch operations in the 3D NAND process flow: (1) channel hole etch, (2) hardmask etch, and (3) silicon nitride recess etch.

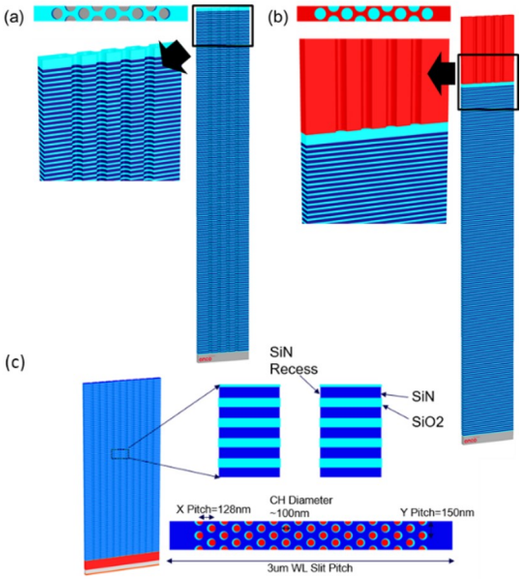

FIG. 1. Representative structures under investigation for the (a) channel hole etch, (b) hardmask etch, and (c) silicon nitride recess applications in 3D NAND memory.

The dominant architecture of 3D NAND memory relies on a silicon dioxide and silicon nitride (ON) superlattice that leverages alternating layers of silicon dioxide and silicon nitride both 25 nm to form vertical stacks that increase storage density the amount of memory increases with the number of layers[57]. These superlattices are critical for charge trapping and insulation in the memory cell architecture. A hexagonal matrix of holes 100 nm must be etched into the ON superlattice ideally with no variation in the diameter of the hole throughout the whole structure. Precise etching of silicon nitride while maintaining selectivity over silicon dioxide is essential to preserve the integrity of the multi-layer through even 1000 layers and avoid defects like oxide redeposition, which can compromise device performance. Advances in etchant chemistry and process control have significantly improved the manufacturability of these complex structures[58,59].

The first two uses cases, (a) and (b), illustrated in Figure 1 relate to the etching of the hexagonal lattice pattern into the ON superlattice. In (b) the pattern is etched into a hardmask layer deposited on top of the ON superlattice and in (a) into the superlattice itself. The hardmask material is amorphous carbon that is used for this application in many semiconduc-

tor manufacturing process flows[60,61]. In (c), the silicon nitride layers are being selectively recessed relative to the silicon dioxide after (b). Provided the holes have a diameter 100 nm and single ON bi-layer is 50 nm, a 100 and 1000 layer structure would have an aspect ratio of 50:1 and 500:1 respectively making measurement of the profile of these structures challenging.

As shown in Figure 2, there is negligible absorption for any wavelength for silicon dioxide and silicon nitride in in the UV-visible-NIR range; however, in the mid-infrared, there are regions of negligible and strong absorption associated with the fundamental Si-O and Si-N bonds.

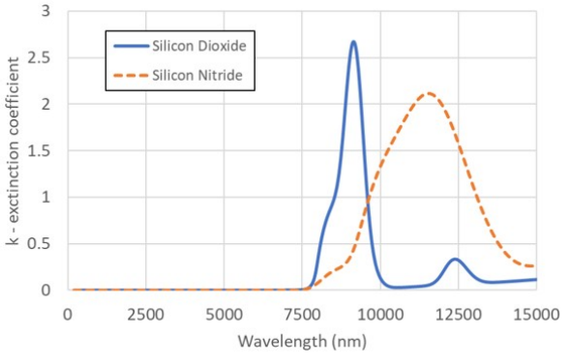

FIG. 2. Optical dispersion curves for PECVD silicon dioxide and silicon nitride measured on a Woollam RC2 and Woollam IR-VASE.

Figure 3 is a finite difference time domain (FDTD) simulation of intensity of the electric field for a set of wavelengths in the mid-infrared range for 192 pair ON tier stack with 100 nm diameter holes illustrated in Figure 1a[36]. This figure demonstrates that light at some wavelengths completely penetrates the whole structure while others are strongly absorbed near the surface. This variation in optical absorption implies that different portions of the structure are sampled by different wavelengths enabling the extraction of the critical dimension of the holes as a function of depth. Figure 3 has only a finite number of absorption snapshots, but the absorption coefficient is continuous as would be the extracted profile. This behavior can be used as a contrast mechanism for measurement of the critical dimensions of these structures.

It is instructive to consider the measured spectra for the UV-visible-NIR and mid-infrared cases shown in Figure 4 (a) and (b) respectively.

Referring to Figure 2, there is little to no absorption for the data in Figure 4 (a). The information relating to the structure exist in the complex high frequency oscillations. In the mid-infrared, there are some low frequency oscillations also derived from thickness fringes, but the absorption imparts a slowly varying structure on the data as well. When applying the RCWA method, an approximation must be made as the series is truncated at a given order. To obtain a good fit to the data, many more orders must be applied to the data in Figure 4 (a) as opposed to the more slowly varying 4 (b) making the former slower to compute. In this instance, the high degree of correlation in the data and the need have a high number of orders to achieve convergence are two strikes against the UV-visible-NIR wavelength range.

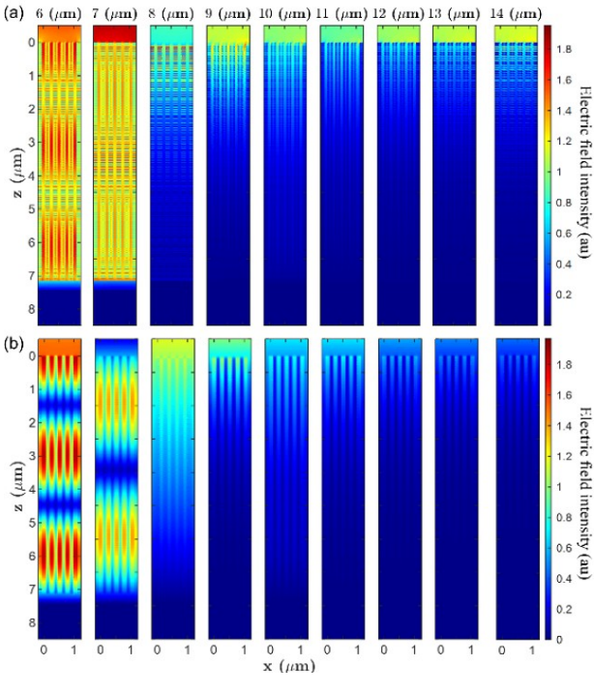

FIG. 3. Electric field intensity for a representative channel hole structures as a function of optical wavelength for TM (a) and TE (b) polarization.

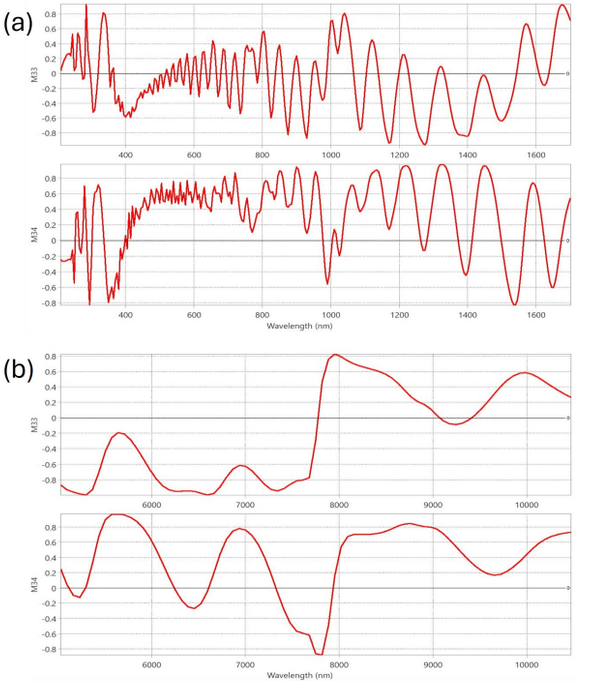

FIG. 4. Measurement of channel-hole structure in (a) UV-visible-NIR on the Onto Innovation Atlas ® V platform and (b) mid-infrared on the Onto Innovation Aspect platform.

In Figure 5, the etched profiles of a given etch process is shown to vary significantly from the center and edge of a 300 mm wafer. The data has been extracted at specific depths based on customer requirement; however, the curve can be defined at arbitrary resolution in depth. The correlation of mid-infrared measured values plotted against a destructive reference for an etch process skew.. The data in this plot is grouped by channel hole diameter for a given depth. The correlation is at the Å-level with typical CD values of 100 nm and the profile averaged repeatability is 0.2% 3-Sigma of the average CD (which corresponds to two Ås for 100nm average CD). The same profile results can be obtained a channel hole etched in an amorphous carbon hardmask film with the mid-infared data agreeing well with a destructive reference[34].The operating principle in this case is the same as in the channel hole etch application. The amorphous carbon films used as hardmasks in these process flows tend to be thick at >4 µm and highly graphitic thus strongly absorbing[61]. The longer absorption length afforded by operating in the mid-infrared makes these measurements possible. Experimental results correlate better than R2 of 0.98 to destructive reference and repeatabilty of the bottom CD is 3.4 Å 3-Sigma.

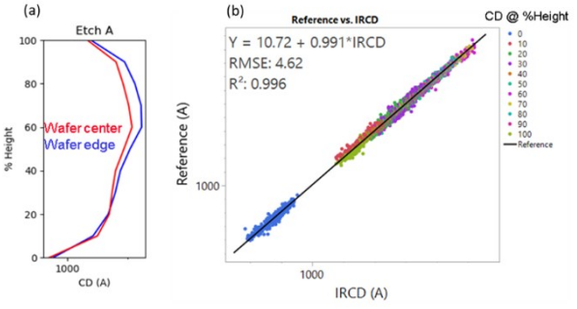

FIG. 5. Measurement of channel-hole profile on an etched ON superlattice in mid-infrared on the Onto Innovation Aspect ® platform.

The lateral silicon nitride recess in the channel hole occurs because of the etch bias between SiO_2 and Si_3N_4. Traditional OCD metrology operating in the UV-visible-NIR range and even x-ray methods are unable to uniquely measure the recess relative to the channel hole due to correlation, however, IRCD (Infrared range OCD) can take advantage of the unique absorption peaks in the mid-infrared to differentiate the channel hole surface from the recessed Si_3N_4 surface. In Keller, et al.[35] the results of mid-infrared data correlation to a destructive reference metrology along with DOE discrimination at the wafer-level with radial dependence plots are presented. Experimental results correlate better than R2 of 0.98 to destructive reference and the average repeatability is roughly 1.5% 3-Sigma (corresponding to sub-Å precision).

The W-Recess etch process in 3D NAND is a critical step in the process flow because it separates adjacent word lines, but in-line process control of this step is not possible using conventional OCD wavelengths because the tungsten render the entire structure opaque. In Keller et. al,[62] IRCD is shown to be able to penetrate down to the bottom of the word line slit, both in FDTD simulations and real experimental data, through the use of design rule compliant target that allows for MIR light to couple to surface plasmon polaritons in the structure. They show that experimental results correlate better than R2 of 0.9 to destructive reference, validating this measurement methodology. The average repeatability is better than 0.8% 3-Sigma (corresponding to Å-level precision).

Deep trench isolation (DTI) trenches are critical structures in power management integrated circuits (PMIC) because they electrically isolate different circuit blocks. Conventional DTI trenches are electrically isolated and can be prone to acting like a floating gate through capacitively coupling to adjacent devices[63]. Newer DTI processes fix this issue by grounding the trench electrically through an additional etch process, but this process requires tight control of the DTI trench profile, specifically the bottom width, because it will determine the contact resistance. IRCD is used to measure the CD profile and utilizes the inherent doping of the Si substrate to modulate the penetration depth of the light in the MIR. Keller et al.[64] show that IRCD is sensitive to the bottom width DOE in three different macros with differing pattern densities. Excellent correlation of IRCD experimental results to cross-sectional SEM reference were achieved, with R2 greater than 0.97 on the three different structures (all with better than 0.1% 3-Sigma precision on BCD, TCD and Depth), showing that IRCD is a viable in-line process control solution for this critical step in the DTI process flow.

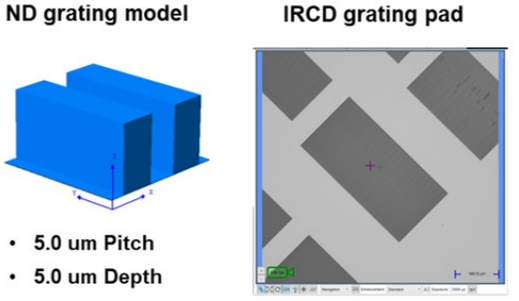

FIG. 6. Grating structure

In the data presented thus far only two Mueller elements have been used. A prototype system capable of measuring eight elements was constructed. More Mueller elements opens the door to considering more complex structures with a greater degree of broken symmetries. As a test case, the large pitch silicon diffraction grating shhown in Figure 6 can be used. When this grating is measured at 0° or 90° relative to the symmetry axis of the grating the off-diagonal elements will be zero assuming the grating is symmetric. Even if there is slightly asymmetry due to the etching process, the off-diagonal elements will at least be very small. However, if the grating is rotated to 45°, the off-diagonal elements will be of the same order as the on-diagonal elements. Figure 7 is measured and modeled result on this structure demonstrating the capability to measure 8 Mueller elements and without any impact on through-put.

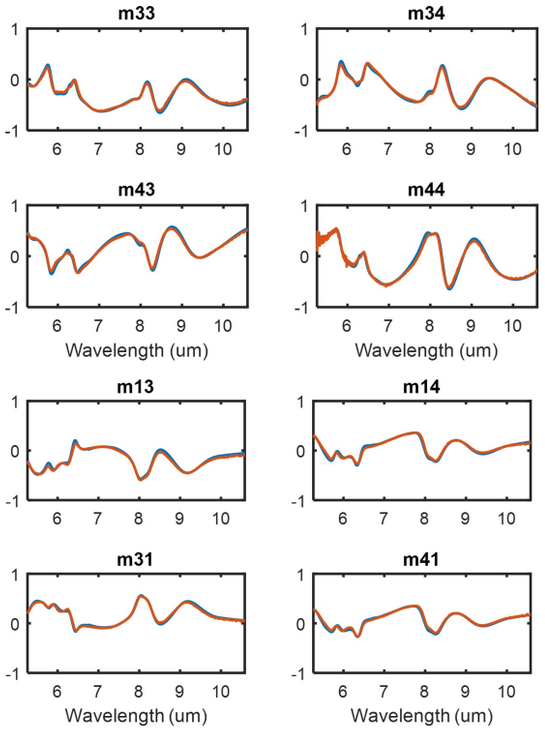

FIG. 7. Measurement versus model for grating structure at 45° on the Onto Innovation Aspect ® platform.

IV. DISCUSSION

The development of mid-infrared ellipsometry for OCD metrology represents a significant advancement in semiconductor process control, particularly for high aspect ratio structures found in 3D NAND architectures. Traditional OCD methods, while effective for many applications, struggle with depth resolution due to limited contrast especially in these ON superlattice structures. The mid-infrared range, by contrast, offers distinct absorption features tied to Si-O and Si-N bonds, enabling selective probing of different layers and depths. The material absorption contrast mechanism levered in 3D NAND can be applied to many other devices through-silicon vias and 3D DRAM being obvious candidates[65–67].

The use of quantum cascade lasers instead of glowbar sources addresses longstanding limitations in signal-to-noise ratio and etendue, making smaller probe sizes and faster acquisition times achievable. The integration of photo-elastic modulators for polarization modulation and lock-in detection enables precise extraction of Mueller matrix elements, with the potential to scale from two to eight elements depending on system configuration. This flexibility supports analysis of both symmetric and asymmetric structures, including rotated gratings and complex etch profiles.

The system modeling approach, grounded in analytical expressions for Stokes vectors and Mueller matrices, provides a robust framework for signal interpretation and calibration. The use of harmonic decomposition and Bessel function ratios to extract retardance and ellipsometric parameters ensures accurate and stable measurements across the spectral range. Moreover, the ability to calibrate the PEM in situ using reflection-based methods enhances long-term reliability and reduces downtime.

Experimental results demonstrate strong correlation between mid-infrared measurements and destructive reference metrology, with sub-Å agreement across multiple etch applications. This validates the technique's utility for monitoring critical dimensions in HAR structures, including channel hole etch, hardmask patterning, and silicon nitride recess. The ability to resolve lateral recess features—previously inaccessible to UV-visible-NIR and x-ray methods—highlights the unique value of mid-infrared absorption contrast.

Finally, the integration of rigorous coupled wave analysis (RCWA) for data modeling ensures accurate reconstruction of complex geometries. While other electromagnetic solvers like FDTD and FDFD are viable, RCWA offers a balance of precision and computational efficiency, particularly when absorption effects dominate. The combination of advanced hardware, robust modeling, and material-specific contrast positions mid-infrared ellipsometry as a critical tool for next-generation semiconductor metrology.

V. CONCLUSION

Mid-infrared ellipsometry, enabled by tunable quantum cascade lasers and polarization modulation, offers a transformative approach to optical critical dimension metrology for advanced semiconductor structures. By leveraging material-specific absorption in the mid-infrared range, this technique provides depth-resolved profiling of high aspect ratio features such as those found in 3D NAND architectures. The ability to extract Mueller matrix elements—initially two and potentially eight with expanded configurations—allows for precise characterization of complex geometries, including asymmetric structures. Calibration methods based on harmonic analysis and Bessel function ratios ensure robust signal interpretation, while integration with rigorous coupled wave analysis (RCWA) enables accurate modeling of patterned structures. Experimental results demonstrate strong correlation with destructive reference metrology across multiple etch applications, validating the method's utility for in-line process control. As semiconductor devices continue to evolve in complexity and scale, mid-infrared ellipsometry stands out as a powerful, non-destructive tool for capturing critical dimensional data with high fidelity and throughput.

[1] Y.-J. Mii, "Semiconductor industry outlook and new technology frontiers," in *2024 IEEE International Electron Devices Meeting* (San Francsico, CA, USA, 2024) p. 1.
[2] S. Mukherjee, D. Pal, A. Bhattacharyya, and S. Roy, "Handbook of semiconductors: Fundamentals to emerging applications," (CRC Press, Boca Rotan, FL, USA, 2024) Chap. 28, pp. 359–374.
[3] N. Orji, R. Dixson, D. Garcia-Gutierrez, B. Bunday, M. Bishop, M. Cresswell, R. Allen, and J. Allgair, "Transmission electron microscope calibration methods for critical dimension standards," J. Micro. Nanolithogr. MEMS MOEMS. **15**, 044002 (2016).

[4]C. Spanos, P. Jula, and R. Leachman, "The economic impact of choosing off-line, inline or in situ metrology deployment in semiconductor manufacturing," in *2001 IEEE International Symposium on Semiconductor Manufacturing. ISSM 2001. Conference Proceedings (Cat. No.01CH37203)* (San Jose, CA, USA, 2001) p. 37.

[5]A. Yamaguchi, R. Nakagaki, and H. Kawada, "CD-SEM technologies for 65-nm process node," Hitachi Review **54**, 15 (2005).

[6]W. Sun, H. Ohta, T. Ninomiya, and Y. Goto, "High-voltage CD-SEM-based application to monitor 3d profile of high-aspect-ratio features," J. Micro. Nanolithogr. MEMS MOEMS. **19**, 024002 (2020).

[7]S. Bukofsky, S. Selberg, R. Grober, and J. Trautman, "Application of near-field optics to critical dimension metrology," Appl. Phys. Lett. **70**, 2368 (2020).

[8]S. Kwon, J. Park, K. Kim, Y. Cho, and M. Lee, "Microsphere-assisted, nanospot, non-destructive metrology for semiconductor devices," Light Sci. App. **11**, 32 (2022).

[9]J. Allgair, D. Benoit, R. Hershey, L. C. Litt, I. Abdulhalim, B. Braymer, M. Faeyrman, J. C. Robinson, U. Whitney, Y. Xu, P. Zalicki, and J. Selingson, "Manufacturing considerations for implementattion of scatterometry for process monitoring," in *Proceedings Volume 3998, Metrology, Inspection, and Process Control for Microlithography XIV* (Santa Clara, CA, USA, 2000) p. 125.

[10]C. Raymond, "Handbook of silicon semiconductor metrology," (CRC Press, Boca Rotan, FL, USA, 2001) Chap. 6, pp. 477–513.

[11]A. Diebold, G. Antonelli, and N. Keller, "Perspective: Optical measurement of feature dimensions and shapes by scatterometry," APL Materials **6**, 058201 (2018).

[12]W. McGahan, B. Spady, J. Iacoponi, and J. Williams, "Combined spectroscopic ellipsometry and reflectometry for advanced semiconductor fabrication metrology," in *Proceedings Volume 2877, Optical Characterization Techniques for High-Performance Microelectronic Device Manufacturing III* (Austin, TX, USA, 1996) p. 1996.

[13]J. Li, J. Hwu, Y. Liu, S. Rabello, Z. Liu, and J. Hu, "Mueller matrix measurement of asymmetric gratings," J. Micro. Nanolithogr. MEMS MOEMS. **9**, 041305 (2010).

[14]H. Tompkins and W. McGahan, *Spectroscopic Ellipsometry and Reflectometry: A User's Guide* (John Wiley and Sons, New York, NY, USA, 1999).

[15]S. Zolner, "Ellipsometry at the nanoscale," (Springer, Berlin, Germany, 2013) Chap. 18, pp. 607–627.

[16]D. Shaughnessy, S. Krishnan, L. Wei, and A. Shchegrov, "Enhancing scatterometry CD signal-to-noise ratio for 1x logic and memory challenges," in *Metrology, Inspection, and Process Control for Microlithography XXVII*, Vol. 8681 (San Jose, CA, USA, 2013) p. 86810V.

[17]S. Lerner and B. Dahlgrenn, "Etendue and optical system design," in *Proceedings Volume 6338, Nonimaging Optics and Efficient Illumination Systems III* (San Diego, CA, USA, 2006) p. 633801.

[18]P. R. Griffiths, "Fourier transform infrared spectrometry," Science **222**, 297 (1983).

[19]T. Pampalone, A. Gilfillan, and P. Zanzucchi, "Fourier transform infrared (FTIR) analysis of photoresist films on silicon wafers," J. Eletrochem. Soc. **133**, 1917 (1986).

[20]A. Grill and D. Neumayer, "Structure of low dielectric constant to extreme low dielectric constant sicoh films: Fourier transform infrared spectroscopy characterization," J. Appl. Phys. **94**, 6697 (2003).

[21]P. Rosenthal, S. Bosch-Charpenay, J. Xu, V. Yakovlev, and P. Solomon, "Advanced FTIR technology for the chemical characterization of product wafers," in *AIP Conf. Proc. 550* (San Francsico, CA, USA, 2001) p. 553.

[22]R. Moellering, L. Bauer, and C. Balestra, "Epitaxial layer thickness measurements using fourier transform infrared spectroscopy (ftir)," J. Electron. Mater. **19**, 181 (1990).

[23]P. Rosenthal, C. Duran, J. Tower, A. Mazurenko, U. Mantz, P. Weidner, and A. Kasic, "Model-based infrared metrology for advanced technology nodes and 300 mm wafer processing," in *AIP Conf. Proc. 788* (Richardson, TX, USA, 2005) p. 620.

[24]T. Kagalwala, B. Erwin, V. Calero-DdelC, Y. Brovman, and L. Höglund, "Mbir characterization of photosensitive polyimide in high volume manufacturing," in *25th Annual SEMI Advanced Semiconductor Manufacturing Conference* (Saratoga Springs, NY, USA, 2014) p. 46.

[25]C. Duran, A. Maznev, G. Merklin, A. Mazurenko, and M. Gostein, "Infrared reflectometry for metrology of trenches in power devices," in *2007 IEEE/SEMI Advanced Semiconductor Manufacturing Conference* (Stresa, Italy, 2007) p. 175.

[26]D. L. Cunf, L. Höglund, and N. Laurent, "In-line metrology of high aspect ratio structu with mbir technique," in *2011 IEEE/SEMI Advanced Semiconductor Manufacturing Conference* (Saratoga Springs, NY, USA, 2011) p. 1.

[27]W. Zhang, J. Xu, S. Wang, Y. Zhou, and J. Mi, "Metrology challenges in 3D NAND flash technical development and manufacturing," J. Microelectron. Manf. **3**, 20030102 (2020).

[28]A. Röseler, "Handbook of ellipsometry," (William Andrew, Inc., Norwich, NY, USA, 2005) Chap. 6, pp. 763–798.

[29]H. Tompkins, T. Tiwald, C. Bungay, and A. Hooper, "Use of molecular vibrations to analyze very thin films with infrared ellipsometry," J. Phys. Chem. B **108**, 3777 (2004).

[30]M. Schubert, *Infrared Ellipsometry on Semiconductor Layer Structures: Phonons, Plasmons, and Polaritons* (Springer, New York, NY, USA, 2004).

[31]J. Benziger, R. Preston, and G. Schoofs, "Considerations in building a low-noise reflection absorption infrared spectrometer," Appl. Optics **26**, 343 (1987).

[32]D. J. Lahneman, T. Huffman, P. Xu, S. Wang, T. Grogan, and M. Qazilbash, "Broadband near-field infrared spectroscopy with a high temperature plasma light source," Opt. Express **25**, 20421 (2017).

[33]W. Miller and R. Smith, "Synchrotrons versus globars, point-detectors versus focal plane arrays: Selecting the best source and detector for specific infrared microspectroscopy and imaging applications," Vib. Spectrosc. **38**, 237 (2005).

[34]G. Antonelli, N. Keller, T. Ribaudo, F. Wong, W. Ming, H. Ding, Z. Chen, R. Grynko, A. Fumani, Z. Liu, S. Takabayashi, J. Hauck, J. Frederick, D. Engelhard, B. Ng, B. Ong, and L. Liong, "Enhancing scatterometry CD signal-to-noise ratio for 1x logic and memory challenges," in *Metrology, Inspection, and Process Control for Semiconductor Manufacturing XXXV*, Vol. 11611 (San Jose, CA, USA, 2021) p. 116111O.

[35]N. Keller, W. Ming, Z. Chen, G. Antonelli, T. Ribaudo, Z. Liu, S. Takabayashi, J. Hauck, J. Frederick, and D. Engelhard, "Novel inline on-device measurement of silicon nitride lateral recess post channel hole ACI with IRCD metrology," in *Metrology, Inspection, and Process Control for Semiconductor Manufacturing XXXVI*, Vol. 12053 (San Jose, CA, USA, 2022) p. 120530T.

[36]A. Fumani, B. Yan, N. Keller, G. Antonelli, and T. Ribaudo, "Decorrelation of optical critical dimensions in mid-infrared ellipsometric spectroscopy of high aspect ratio etch profiles," J. Micro/Nanopattern. Mater. Metrol. **21**, 021205–1 (2022).

[37]G. Antonelli and T. Ribaudo, U.S. Patent No. 10,901,241 (26 Jan. 2021).

[38]B. Barner, M. Green, E. Saez, and R. Corn, "Polarization modulation fourier transform infrared reflectance measurements of thin films and monolayers at metal surfaces utilizing real-time sampling electronics," Anal. Chem. **63**, 55 (1991).

[39]M. Green, B. Barner, and R. Corn, "Real-time sampling electronics for double modulation experiments with fourier transform infrared spectrometers," Rev.Sci. Instrum. **62**, 1426 (1991).

[40]G. Jellison and F. Modine, "Two-channel polarization modulation ellipsometer," Appl. Optics **29**, 959 (1990).

[41]R. Lachance, "Non-linearity correction of FTIR instruments," in *5th Workshop of Infrared Emission Measurements by FTIR* (Québec City, CA, 2000) p. 1.

[42]T. Oakberg, "Using a mechanical chopper with a pem to measure vdc," Tech. Rep. (Hinds Instruments, 2005).

[43]C. Hu, L. Sun, Y. Li, M. Hohage, J. Flores-Camacho, X. Hu, and P. Zeppenfeld, "Retardation correction for photoelastic modulator-based multichannel reflectance difference spectroscopy," J. Opt. Soc. Am. A **25**, 1240 (2008).

[44]G. Jellison and F. Modine, "Two-modulator generalized ellipsometry: experiment and calibration," Appl. Optics **36**, 8184 (1997).

[45]G. Jellison and F. Modine, "Two-modulator generalized ellipsometry: theory," Appl. Optics **36**, 8190 (1997).

[46]O. Arteaga, J. Freudenthal, B. Wang, and B. Kahr, "Mueller matrix polarimetry with four photoelastic modulators: theory and calibration," Appl. Optics **51**, 6805 (2012).

[47]G. Jellison, "Windows in ellipsometry measurements," Appl. Optics **38**, 4784 (1999).

[48]G. Antonelli, T. Ribaudo, and M. Hammond, U.S. Patent No. 11,162,897 (2 Nov. 2021).
[49]Wolfram Research, Inc., "Mathematica, Version 14.3," Champaign, IL, 2025.
[50]M. Moharan and T. Gaylord, "Rigorous coupled-wave analysis of planar-grating diffraction," J. Opt. Soc. Am. **71**, 811 (1981).
[51]L. Li, "Fourier modal method for crossed anisotropic gratings with arbitrary permittivity and permeability tensors," J. Opt. A: Pure Appl. Opt. **5**, 345 (2003).
[52]M. Foldyna, K. Postava, D. Ciprian, and J. Pištora, "Modeling of magneto-optical properties of periodic nanostructures," J. Magn. Magn. Mater. **290-291**, 120 (2005).
[53]M. Foldyna, R. Ossikovski, A. D. Martino, B. Drevillon, K. Postava, D. Ciprian, J. Pištora, and K. Watanabe, "Normal vector method for convergence improvement using the rcwa for crossed gratings," J. Opt. Soc. Am. A **24**, 2880 (2007).
[54]R. Rumpf, *Design and optimization of nano-optical elements by coupling fabrication to optical behavior*, Doctoral dissertation, University of Central Florida (2006).
[55]R. Rumpf, *Electromagnetic and Photonic Simulation for the Beginner: Finite-Difference Frequency-Domain in MATLAB* (Artech House, Nrowood, MA, USA, 2022).
[56]P. Vagos, J. Hu, Z. Liu, and S. Rabello, "Uncertainty and sensitivity analysis and its applications in ocd measurements," in *Metrology, Inspection, and Process Control for Microlithography XXIII*, Vol. 7272, edited by J. A. Allgair and C. J. Raymond, International Society for Optics and Photonics (SPIE, 2009).
[57]H. Tanaka, M. Kido, K. Yahashi, M. Oomura, R. Katsumata, M. Kito, Y. Fukuzumi, M. Sato, Y. Nagata, Y. Matsuoka, Y. Iwata, H. Aochi, and A. Nitayama, "Bit cost scalable technology with punch and plug process for ultra high density flash memorys," in *2007 IEEE Symposium on VLSI Technology* (Kyoto, Japan, 2007) p. 14.
[58]T. Lill and A. Fischer, "Semiconductor dry etching innovation in the era of 3d monolithic integration," Electrochem. Soc. Interface **33**, 69 (2024).
[59]T. Park, J. Han, and S. Lim, "Selective si_3n_4 etching for 3D NAND integration by using low concentration of h_3po_4," SSP **346**, 137 (2023).
[60]W.-Y. Jung, S.-M. Kim, C.-D. Kim, G.-H. Sim, S.-M. Jeon, S.-W. Park, B.-S. Lee, S.-K. Park, J.-S. Kim, and L.-S. Heon, "Patterning with amorphous carbon spacer for expanding the resolution limit of current lithography tool," in *Proceedings Volume 6520, Optical Microlithography XX* (San Jose, CA, USA, 2007) p. 65201C.
[61]G. A. Antonelli, S. Reddy, P. Subramonium, J. Henri, J. Sims, J. O'loughlin, N. Shamma, D. Schlosser, T. Mountsier, and W. Guo, "Patterning with amorphous carbon thin films," ECS Trans. **35**, 701 (2011).
[62]N. Keller, Z. Chen, P. Wang, R. Grynko, T. Ribaudo, G. A. Antonelli, Y. Wang, J. Frederick, S. Takabayashi, J. Hauck, and D. Engelhard, "Measurement of W-recess profile in advanced node 3D NAND device with IRCD technology utilizing a specialized design-rule compliant target," in *Metrology, Inspection, and Process Control XXXVII*, Vol. 12496, edited by J. C. Robinson and M. J. Sendelbach, International Society for Optics and Photonics (SPIE, 2023) p. 124961Z.
[63]S. H. Voldman, "The influence of a novel contacted polysilicon-filled deep trench (dt) biased structure and its voltage bias state on cmos latchup," in *2006 IEEE International Reliability Physics Symposium Proceedings* (2006) pp. 151–158.
[64]N. Keller, M. Poulingue, R. Grynko, T. Ribaudo, G. A. Antonelli, V. Li, M. Ravasio, and D. L. Cunff, "Non-destructive measurement of bottom width in deep trench isolation structures using IRCD metrology," in *Metrology, Inspection, and Process Control XXXVIII*, Vol. 12955, edited by M. J. Sendelbach and N. G. Schuch, International Society for Optics and Photonics (SPIE, 2024) p. 1295514.
[65]J. U. Knickerbocker *et al.*, "3d silicon integration," in *58th Electronic Components and Technology Conference* (Lake Buena Vista, FL, USA, 2008) pp. 538–543.
[66]D. Malta *et al.*, "Fabrication of TSV-based silicon interposers," in *2010 IEEE International 3D Systems Integration Conference (3DIC)* (Munich, Germany, 2010) pp. 1–6.
[67]K. Choi, S. Kim, J. Seo, H. Kang, S. Chu, and S. Bae, "A three dimensional dram (3d dram) technology for the next decades," in *2024 IEEE Symposium on VLSI Technology and Circuits* (Honolulu, HI, USA, 2024) pp. 1–2.